MDPI

Article

Integrated Design and Flight Validation of Solar-Powered Unmanned Aerial Vehicle (UAV) Structure and Propulsion System

Qing Guo *[ID]**, Minghao Qiu *, Xiaoqiang Li, Wen Sun and Zihua Guo**

School of Aeronautics, Northwestern Polytechnical University, Xi'an 710072, China; lxq010317@163.com (X.L.); pajaman@163.com (W.S.); gzih@mail.nwpu.edu.cn (Z.G.)

* Correspondence: gq@nwpu.edu.cn (Q.G.); qmhnwpu@163.com (M.Q.)

Abstract: The development of solar-powered unmanned aerial vehicles (UAVs) primarily focuses on enhancing the efficiency of the propulsion system to minimize energy consumption during the conversion of valuable solar energy. However, due to the unique nature of UAV propulsion systems, there is limited cross-reference ability among existing solar-powered UAV systems. This paper proposes an integrated design approach for the propulsion system and UAV structure. Based on this approach, an overall design is conducted for the solar-powered UAV, including initial design goals and performance parameters. Aerodynamic layout design and performance estimation are carried out, and a prototype is fabricated and assembled for flight testing validation. The results demonstrate the significant importance of this approach in improving the efficiency of the solar-powered UAV propulsion system.

Keywords: solar-powered UAV; integrated design; aerodynamic optimization design; flight testing

1. Introduction

1.1. Concept of Integrated Design

A solar-powered unmanned aerial vehicle (UAV) is composed of four major components: the airframe, propulsion system, energy system, and onboard equipment. The propulsion system includes the motor and its controller, gearbox, propeller, and thrust control mechanism. The overall performance of a UAV is the result of the coordinated operation of these components. The relationship between the UAV and its propulsion system is particularly crucial. In the development process of UAVs, the continuous improvement in engine performance has played a determining role in enhancing UAV performance, and for solar-powered UAVs, the connection between the engine and the aircraft is even more inseparable. The engine's performance should be evaluated and designed in conjunction with the UAV. Solar-powered UAVs have the characteristics of low wing loading, slow speed, and low power requirements, demanding high efficiency and reliability from the propulsion system [1]. The solar-powered UAV and its propulsion system are closely linked in terms of aerodynamics, structure, performance, and operation. Therefore, in the design of solar-powered UAVs and their propulsion systems, the coordination and compatibility between the UAV and the propulsion system must be taken into consideration, including the considerations of UAV performance requirements and the mutual influence between the UAV and the propulsion system [2]. Therefore, it is necessary to conduct comprehensive parameter optimization for the airframe and propulsion system, referred to as the integrated design of a UAV/propulsion system.

1.2. Integrated Design Work of the Solar-Powered UAV

The integrated design of the solar-powered unmanned aerial vehicle (UAV) body and power system is conducted from the perspective of the entire UAV system, encompassing research and design of the UAV, solar panels, and power system. Leveraging past

UAV design practices and the characteristics of solar-powered UAVs [3]. an analytical approach based on aerodynamics and performance analysis is employed for the UAV body design [4–8]. This approach is typically an engineering method used to assess and design aircraft, grounded in the theoretical foundations of aerodynamics and performance analysis. It aids in clearly illustrating the principles of solar-powered UAV design and optimization, facilitating optimization, integration, trade-offs, and balance, with the aim of overall efficiency. This approach allows for comprehensive analysis and integrated optimization design in various aspects such as structure, strength, aerodynamics, thermodynamics, control, reliability, usability, maintenance, and lifetime cost, ultimately enhancing the efficiency of the power system [9]. Furthermore, it is suitable for the early design stages and can provide quick preliminary results, serving as a validation method for the integrated design of the solar-powered UAV body and power system. In future research, further optimization of the solar-powered UAV's airframe can be conducted using computational fluid dynamics (CFD) methods [10–15], particularly in addressing complex fluid dynamics issues, including turbulence, three-dimensional flow, and multiphase flow [16]. In the preliminary design stage, it is essential to determine the overall parameters of the UAV, including wing area and flight speed, while considering the efficiency and characteristics of the energy management system. It involves estimating the energy provided to the power system and selecting a motor and gearbox compromise based on energy characteristics and propeller considerations. Furthermore, the choice of a propeller depends on the torque and speed characteristics of the gearbox output shaft, the UAV's flight performance, and energy characteristics.

1.3. Main Contributions of This Paper

This paper illustrates the integrated design of the UAV propulsion system through the example of a 3 kg solar-powered UAV. The wingspan of the UAV, designed to be approximately 6 m, can be used to test the performance of large aircraft using scaled-down validation methods [17–19]. This paper showcases the layout design and selection of the UAV, the optimization of propeller power requirements, and the theoretical design process. Relevant software and acquired knowledge are utilized in the design of the wings, fuselage, and tail, as well as in the estimation of UAV performance. Subsequently, a prototype is fabricated, and results obtained through prototype test flights are used to validate the performance of the UAV, ensuring that the UAV's airframe design precisely matches the output of the power system. This approach demonstrates the feasibility of such methods in the field of aircraft design.

2. Layout Design

2.1. Power System

Solar-powered unmanned aerial vehicles (UAVs) without energy storage units typically fly using the maximum power output of the solar panels throughout the entire flight [20,21]. The validation aircraft used in this study lacks an energy storage unit. The existing power tracking and power management system is designed to control the output of the solar panel array based on various mission profiles of the aircraft, taking into account the required maximum power and energy for different flight profiles and local solar time [22]. This ensures that the solar panel array delivers the maximum power output for various mission profiles. Table 1 illustrates the maximum output power for each mission profile. Experimental measurements indicate that the power of the 72 solar panels is 120 W, which meets the power requirements for the 3 kg empty-weight UAV. The motor selected is the Dualsky XM2826EA-12, with a KV value of 1370 rpm and a reduction ratio of 15.2. The power rating of the propulsion system is small at 120 W. Based on the reduction ratio of 15.2, a two-stage gear reduction system is chosen. Gear reduction systems offer high transmission efficiency, low energy consumption, and superior performance [23]. It can meet the requirements of high efficiency, low weight, and the desired reduction ratio for the solar-powered UAV. The propeller consists of a low vortex drag propeller created

based on elliptical wing theory [24,25], which possesses a good thrust-to-weight ratio and high efficiency. However, it is sensitive to the free-stream velocity and will experience a significant decrease in performance within a certain range as the free-stream velocity increases. Considering that solar-powered UAVs are designed with characteristics resembling gliders, such as low wing loading and low flight speeds [26], this propeller is suitable for solar-powered UAVs.

Table 1. The maximum output power for each mission profile.

Mission Profile	Maximum Output Power	Units
Climb Phase	120	w
Level Flight Phase	40	w
Landing Phase	30	w

2.2. Layout Configuration

The aerodynamic layout adopts a conventional configuration. The conventional configuration can design satisfactory low-speed performance and is easy to maneuver. It also facilitates the planning of solar panels. The conventional configuration has a simple structure, mature technology, and well-established design methods [27]. The UAV adopts a mid-wing layout. The mid-wing layout helps reduce interference drag, but the main consideration here is that the mid-wing layout is advantageous for connecting the segmented wings with the fuselage, and it also reduces the load transfer path [28]. The UAV's propulsion system adopts a single-pull configuration. A single engine has advantages such as higher efficiency and lighter weight compared to multiple engines. Placing the engine at the front of the aircraft is beneficial for the balance of the solar-powered UAV. The horizontal stabilizer of the UAV is located at the rear of the fuselage, while the elevator is positioned at the root of the vertical stabilizer. The horizontal and vertical stabilizers have a small angle of sweep, which helps increase the moment arm of the tail and improve the lift curve slope of the tail, thereby enhancing the efficiency of the tail [29]. Additionally, the sweep of the tail surfaces is a common design style. The UAV does not intend to use landing gear, as landing gear would increase drag and structural weight. Solar-powered UAVs do not require frequent short-term takeoffs, so they can take off with the assistance of a launch vehicle. The launch vehicle is not fixed to the aircraft and will automatically detach during the taxi phase. The landing method involves a belly landing.

2.3. Design Requirements

In consideration of the solar panel coverage area and wing loading, the wing area can be preliminarily determined [30]. Taking into account construction and transportation conditions, each non-removable component should not exceed 2.4 m. The lift is directly related to the amount of sunlight, and the maximum takeoff weight can reach up to 8 kg, varying with sunlight conditions. Table 2 presents the design requirement parameters.

Table 2. Design requirement parameters.

Requirements	Numerical Values	Units
Wingspan (A)	>5	m
Size of non-disassemblable components	<2.4	m
Reference value of thrust	9.8	N
UAV empty weight	3–8	kg
Wing loading	2.66	kg/m^2
Wing area	3.0086	m^2
Design flight speed	7.5	m/s
Target lift-to-drag ratio	15	
Climb rate	0.3	m/s
Number of solar panels	>72	

2.4. Wing Design

2.4.1. Selection of Airfoil

Taking into account the characteristics of low speed and low thrust-to-weight ratio in solar-powered UAVs [31], the selection of airfoils should prioritize low drag coefficients and high lift-to-drag ratios under low Reynolds numbers (300,000). Additionally, factors such as structural design complexity and trim considerations should be taken into account, favoring airfoils with greater thickness and lower moment coefficients [32]. Preliminary screening of airfoils in the Profili airfoil database is conducted within the thickness range of 10% to 14% and camber range of 3% to 8% under a Reynolds number of 300,000 [33]. Among the selected candidates, including MH115, SD-7032-099-88, E214, Eppler67, and FX63-110, a detailed comparison is carried out regarding polar curves, lift-to-drag ratios, drag coefficients, and moment coefficients. Finally, the MH115 airfoil is chosen. Figure 1 depicts the airfoil performance of MH115.
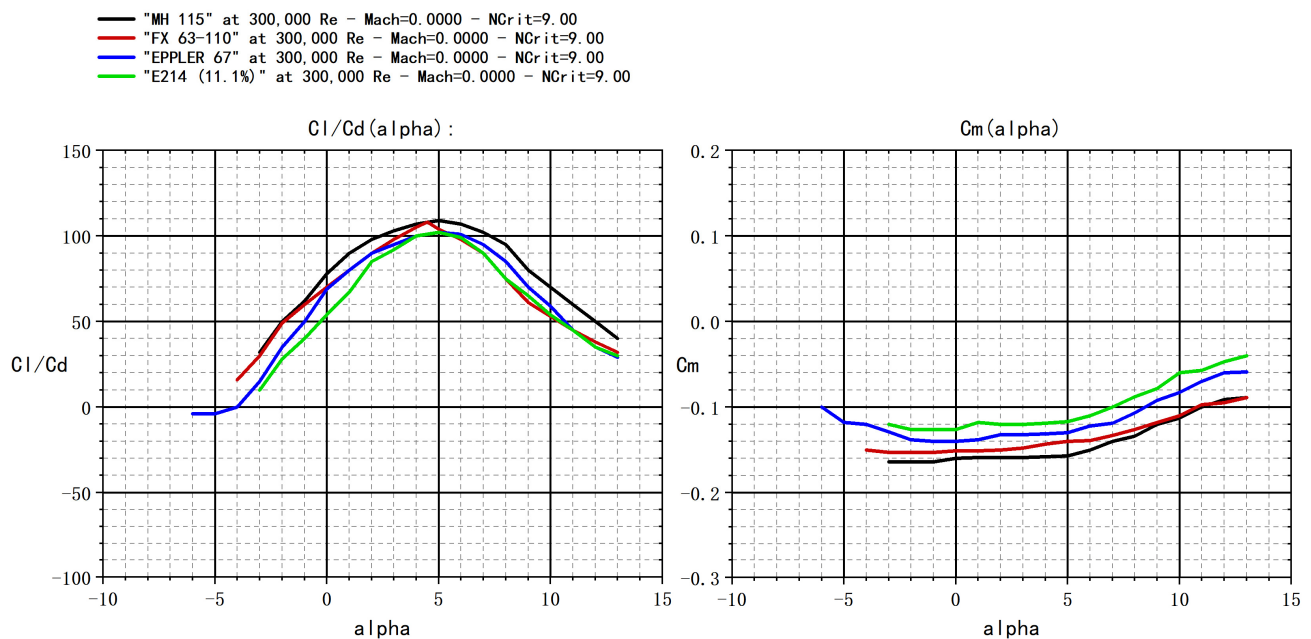

Figure 1. Airfoil MH115: max thickness 11.07% at 29.8% of the chord.

2.4.2. Geometric Parameters

The geometric shape of the wing is depicted in Figure 2. The wing is the primary surface for solar radiation capture, and a flat wing maximizes the surface area exposed to sunlight [34]. An elliptical shape minimizes induced drag, but considering manufacturing complexity, a trapezoidal wing is optimal. To strike a balance between energy and aerodynamic performance, a combination of trapezoidal and flat sections is adopted for the wing's geometry [35]. The flat section has a span of 1.747 m and a chord length of 0.545 m. The first trapezoidal section has a span of 0.688 m and a taper ratio of 0.48794 m. The second trapezoidal section has a span of 0.465 m and a taper ratio of 0.3815 m. The spar remains straight and is located at 32.29% of the root chord, primarily considering the effects of solar panel installation. The leading edge sweep is 9°, and the trailing edge sweep is 5°. Table 3 presents the geometric parameters of the wing.
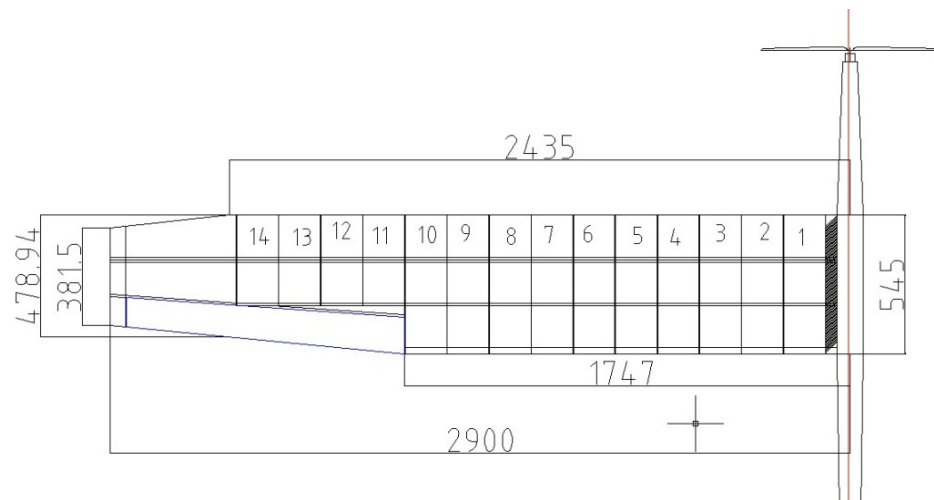
Figure 2. Geometric schematic of the wing.

Table 3. Geometric parameters of the wing.

Parameter Name(s)	Numerical Values	Units
Wing area (S_w)	3.0086	m^2
Fuselage area as a percentage of the wing area (S_b)	0.0545	m^2
Wingspan length (b_w)	5.8	m
Aspect ratio (b_w^2/S_w)	11.8	
Effective aspect ratio (A_e)	10.98	
Root taper ratio (λ_w)	0.6	

2.4.3. Mean Aerodynamic Chord

The expression for the average aerodynamic chord length of a complex-shaped wing, as shown in Figure 3, can be written as follows [36]:

$$c_A = \frac{2}{S} \int_0^{\frac{b_w}{2}} c^2(z)\,dz \tag{1}$$
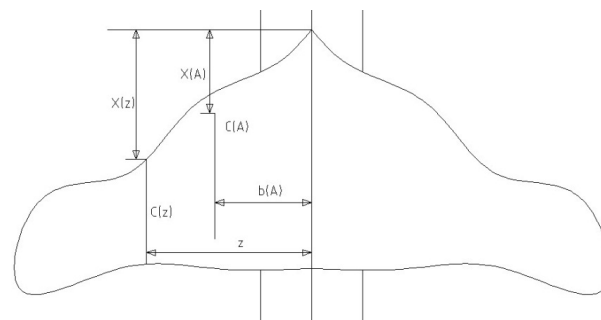

Figure 3. Complex wing geometry.

The expression for the position of the average aerodynamic chord length can be written as follows:

$$b_A = \frac{2}{S} \int_0^{\frac{b_w}{2}} z\,c(z)\,dz \tag{2}$$

$$x_A = \frac{2}{S} \int_0^{\frac{b_w}{2}} x(z)\,c(z)\,dz \tag{3}$$

$c(z)$ represents the chord length distribution along the span, and $x(z)$ represents the distribution of the distance between the leading edge of the chord line and the leading edge of the root chord along the span.

For the wing designed in this context, the expressions are as follows:

$$\begin{cases} c(z) = 0.545, & 0 < z < 1.747 \\ c(z) = 0.71274 - 0.096z, & 1.747 < z < 2.435 \\ c(z) = 0.9892 - 0.209548z, & 2.435 < z < 2.9 \end{cases} \tag{4}$$

$$\begin{cases} x(z) = 0, & 0 < z < 2.435 \\ x(z) = 0.113548z - 0.27649, & 2.435 < z < 2.9 \end{cases} \tag{5}$$

According to the calculation from the above formula, we obtain c_A as 0.52247 m, b_A as 1.39436 m, and x_A as 0.003378 m. The aerodynamic center of the wing is located at a distance of 0.134 m behind the leading edge of the root rib, which can be calculated as $0.52247 \times 0.25 + 0.003378 = 0.134$ m.

2.4.4. Wing Lift Slope

The expression for the lift curve slope of an isolated airfoil in incompressible flow can be written as follows:

$$C_L^\alpha = \frac{2\pi A_e}{2 + \sqrt{4 + \left(\frac{A_e}{cos\Lambda_{1/2}}\right)^2}} \tag{6}$$

The theoretical value for the lift curve slope of an airfoil is 2π, but for thicker airfoils, it increases with an increase in thickness (c) and trailing edge thickness ratio (τ). The experimental value is approximately $0.9 \times 2\pi$ [37]. Taking the thickness correction into account, the expression can be modified as follows:

$$C_{y\infty}^\alpha = 1.8\pi(1 + 0.8c) \tag{7}$$

The lift curve slope of a wing is smaller than that of an individual airfoil and is approximately

$$C_y^\alpha = C_{y\infty}^\alpha / \left(1 + \frac{C_{y\infty}^\alpha}{\pi A_e}\right) \tag{8}$$

For the main wing with the MH115 airfoil, having a thickness of 11.08% and an effective aspect ratio (A_e) of 10.98, the lift curve slope (C_y^α) can be calculated as 1.6628π.

2.5. Fuselage Design

Figure 4 represents a schematic diagram of the fuselage geometry. The fuselage is slender in shape, and to ensure a sufficient tail moment arm, the distance from the rear of the fuselage to the leading edge of the wing is 2 m. Considering construction and transportation conditions, the length of the fuselage is 2.6 m. At the wing junction, the fuselage cross-section measures 0.1 m $\times$ 0.1 m, tapering down to 0.06 m $\times$ 0.06 m towards the front and rear.
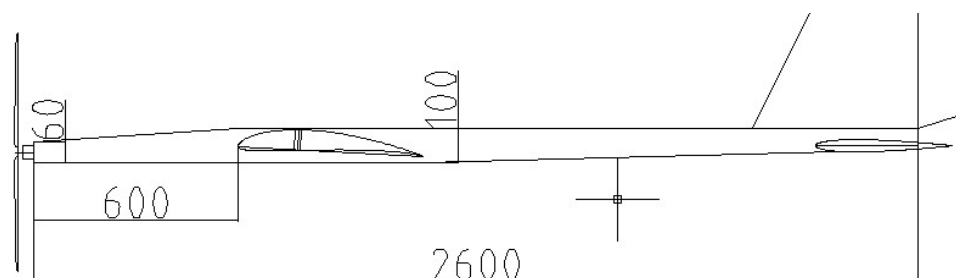

Figure 4. Geometric schematic of the fuselage.

The volume of the cabin is 5000 cm^3, and the cross-sectional area inside the wing is 81 cm^2. The length of the cabin is 0.61 m, and it is symmetrically placed around the center of gravity.

2.6. Tail Design

2.6.1. Horizontal Tail Design

Figure 5 represents a schematic diagram of the horizontal tail. The aspect ratio of the horizontal tail should be smaller than that of the main wing. For this UAV, the aspect ratio of the main wing is greater than 10. Based on statistical data for modern UAVs [38], the aspect ratio of the horizontal tail is typically between 3.5 and 4.5. Here, we choose a value of $A_h = 3.5$ and a taper ratio of $\lambda_h = 0.8$ for the horizontal tail. The leading edge is swept to ensure a straight trailing edge. The root chord of the horizontal tail is set as 0.4 m, with a span of 1.26 m and an area of 0.4536 m^2. The leading edge of the horizontal tail is located 1.70 m from the leading edge of the main wing. The elevator has a span of 1.14 m and a chord length of 0.1 m, representing 24% of the total horizontal tail area. The elevator can deflect upwards at an angle of 25° and downwards at an angle of 20°. Table 4 provides the geometric parameters of the horizontal tail.
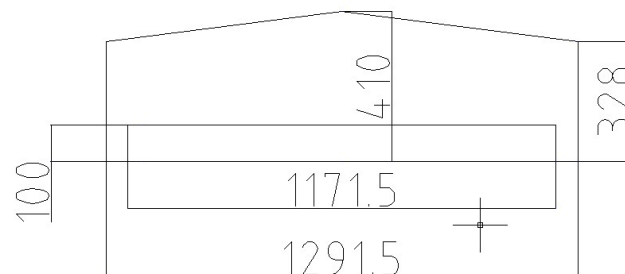

Figure 5. Geometric schematic of the horizontal tail.

Table 4. Horizontal tail geometric parameters.

Name(s)	Numerical Values	Units
Horizontal tail aspect ratio (A_h)	3.5	
Horizontal tail taper ratio (λ_h)	0.8	
Horizontal tail root chord length (c_r)	0.4	m
Horizontal tail span length (b_h)	1.26	m
Horizontal tail area (S_h)	0.4536	m^2
Horizontal tail tip chord length (c_t)	0.328	m
Elevator span length	1.14	m
Elevator chord length	0.1	m
Elevator up angle	25	°
Elevator down angle	20	°

The average chord length of a simple trapezoidal wing can be calculated using a simple formula:

$$c_{A_h} = \frac{4}{3} \frac{s_h}{b_h} \left[1 - \frac{\lambda_h}{(1 + \lambda_h)^2} \right] \tag{9}$$

$$b_{A_h} = \frac{b_h}{6} \frac{1 + 2\lambda_h}{1 + \lambda_h} \tag{10}$$

$$x_{A_h} = b_{A_h} \tan(\Lambda_0) \tag{11}$$

$$\tan(\Lambda_0) = \frac{2(c_r - c_t)}{b_h} \tag{12}$$

The distance between the aerodynamic center of the horizontal tail and the leading edge is 0.132 m, located at position 1.822 m. Using XFLR5 V6.47 software, the suitable

center of gravity position is found to be $X_{OG} = 0.195$ m. Thus, the length of the tail moment arm (L_h) is 1.634 m. The expression for the tail volume is as follows:

$$C_h = \frac{S_h L_h}{S_w c_A} \tag{13}$$

The value of C_h is determined to be 0.4715, and the ratio of the horizontal tail area to the wing area is $S_h / S_w = 0.1584$. The airfoil used for the horizontal tail is NAC 0009, with a lift curve slope of approximately $0.99 \times 2\pi$. However, considering the limited aspect ratio, the lift curve slope is taken as 1.24π.

The distance between the aerodynamic center of the wing (0.134 m) and the aerodynamic center of the horizontal tail is 1.688 m.

The lift curve slopes for the main wing and the horizontal tail are $C_y^\alpha = 1.6628\pi$ and $C_{yht}^\alpha = 1.24\pi$, respectively. When the angle of attack increases by $\Delta\partial$, the increase in lift can be calculated as follows: $0.5\rho v^2 S_w C_y^\alpha \Delta\partial$ for the main wing and $0.5\rho v^2 S_h C_{yht}^\alpha \Delta\partial \times 0.8$ for the horizontal tail while considering the flow blockage from the main wing and assuming the lift of the horizontal tail is 80% of its original value. From the above analysis, the distance (x) of the lift increment action point from the aerodynamic center of the main wing can be expressed as follows:

$$x \left(0.5\rho v^2 S_w C_y^\alpha \Delta\partial + 0.5\rho v^2 S_h C_{yht}^\alpha \Delta\partial \times 0.8 = 1.688 \times 0.5\rho v^2 S_h C_{yht}^\alpha \Delta\partial \times 0.8 \right. \tag{14}$$

The calculation yields x = 0.146, indicating that this position is located at $X_{NP} = 0.280$ of the root chord. This position is also the overall aerodynamic center, which is located at 52.94% of the mean aerodynamic chord (MAC).

2.6.2. Vertical Tail Design

Figure 6 represents a schematic diagram of the vertical tail. The length of the vertical tail moment arm is $L_{VT} = 1.565$ m, and the vertical tail volume coefficient is $C_{VT} = 0.025$.
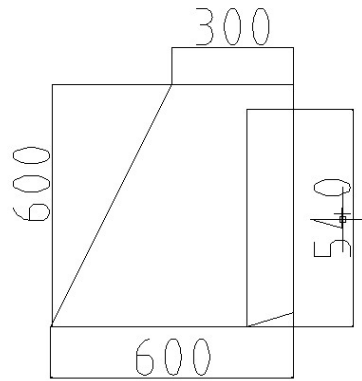

Figure 6. Geometric schematic of the vertical tail.

The expression for the vertical tail area (S_{VT}) is as follows:

$$S_{VT} = \frac{C_{VT} \cdot b_W \cdot S_W}{L_{VT}} \tag{15}$$

Based on statistical data, the vertical tail aspect ratio (A_V) ranges from 0.8 to 1.2, and the taper ratio (λ_V) ranges from 2.0 to 3.5. For this design, let us choose $A_V = 1.3\lambda_V = 2$. The root chord of the vertical tail is 0.6 m, and the tip chord is 0.6 m as well. The leading edge of the vertical tail should have a sweep angle that ensures a straight trailing edge [39]. The rudder (directional control surface) has a chord length of 0.115 m and a span of 0.54 m, with a total area of 0.062 m^2, which accounts for 0.229 of the total vertical tail area. The distance between the aerodynamic center of the vertical tail and the leading edge of the root chord

is 0.250 m. The average aerodynamic chord length of the vertical tail is 0.4666 m, located at 0.2666 m of the span. Table 5 provides the geometric parameters of the vertical tail.

Table 5. Vertical tail geometric parameters.

Name(s)	Numerical Values	Units
Vertical tail aspect ratio (A_V)	2	
Vertical tail taper ratio (λ_V)	0.8	
Vertical tail root chord length (c_v)	0.6	m
Vertical tail area (S_{VT})	0.4536	m^2
Vertical tail moment arm length (L_{VT})	1.565	m
Vertical tail volume (C_{VT})	0.025	
Vertical tail span length (b_v)	0.6	m
Rudder chord length	0.115	m
Rudder span length	0.54	m
Rudder area	0.062	m^2

3. Aerodynamic Performance Estimation

3.1. Lift-Induced Drag

In specific flight conditions, it is commonly believed that the induced drag factor A for the UAV is considered constant [40]. The calculation expression for the induced drag coefficient is as follows:

$$C_{Di} = AC_L^2 \tag{16}$$

In reality, the induced drag factor A does vary with the change in lift coefficient C_L. However, for high aspect ratio UAVs, A can be considered constant within a certain range. The estimation expression for the value of A is as follows:

$$A = 1/(\pi A_e e) \tag{17}$$

A_e represents the effective aspect ratio, and e is the empirical lift efficiency factor. The lift efficiency factor e takes into account the influence of wingspan, fuselage width, and wing taper ratio. Existing statistical data has been fitted into analytic expressions as follows:

$$e = 1 - 0.9876 \left(\frac{b_{fav}}{b_w} \right)^{0.8963} \left(1 - 0.3885\lambda^{0.6991} \right) \tag{18}$$

b_{fav} represents the ratio of the fuselage length to the wingspan. The calculation from the above equation yields A as 0.02955 and e as 0.9811.

3.2. Zero-Lift Drag

The zero-lift drag coefficient, also known as the minimum drag coefficient, refers to the parasitic drag or zero-lift drag that is independent of lift. The numerical calculation methods for the minimum drag coefficient of modern UAVs are quite complex [41]. However, for the purpose of this UAV, the following method can be considered sufficient.

The overall zero-lift drag coefficient can be estimated as follows:

$$C_{DO} = Wetted\ area \times Skin\ friction\ coefficient / Wing\ area \tag{19}$$

The relevant parameters for zero-lift drag are shown in Table 6.

Table 6. Zero-lift drag parameters.

Name(s)	Numerical Values	Units
Wetted area of the fuselage	0.8828	m^2
Wetted area of the wing	6.16588	m^2
Wetted area of the horizontal tail	1.4995	m^2
Total wetted area of the UAV	8.548	m^2
Drag coefficient	0.01	

The overall zero-lift drag coefficient of the aircraft is calculated to be 0.028412. Taking into account the additional drag from the servo actuators and the variable pitch mechanism, a correction factor of 0.003 is added, resulting in a modified value of 0.031412.

3.3. Maximum Lift-to-Drag Ratio

The expression for the drag coefficient is as follows:

$$C_D = C_{D0} + C_{Di} = C_{D0} + AC_L^2 \tag{20}$$

$$C_D = C_{D0} + AC_y^2 = 0.031412 + 0.02955C_y^2 \tag{21}$$

The position of maximum lift-to-drag ratio occurs at $C_{D0} = C_{Di}$, where $0.031412 = AC_L^2$. At this position, C_L is equal to 1.04, resulting in a lift-to-drag ratio of 16.4. At the maximum lift-to-drag ratio, the drag coefficient is 0.0628.

3.4. Lift Characteristics

Figure 7 represents the relationship between the lift coefficient and the angle of attack for the wing. The slope of the lift curve, also known as the lift coefficient derivative with respect to the angle of attack, is equal to $C_y^\alpha = 1.6628\pi$.
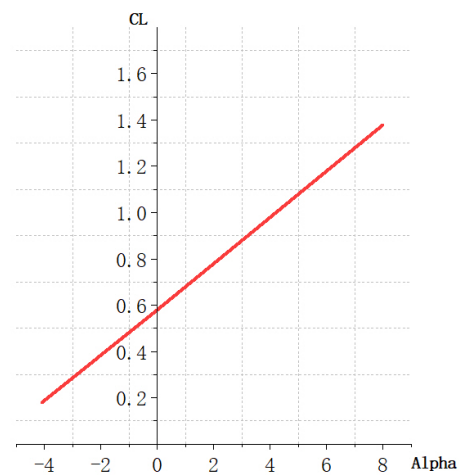
Figure 7. Lift coefficient (CL) versus angle of attack (Alpha) curve for the wing.

The formula for calculating the lift coefficient is as follows:

$$C_L = C_L^\alpha(\alpha - 0) + C_L^0 \tag{22}$$

Considering a maximum lift-to-drag ratio lift coefficient of 1.04 (C_L), a lift coefficient slope of 0.09117 (C_L^α), and a zero angle of attack lift coefficient of 0.52 (C_L^0), the calculated installation angle is determined to be 2.59°. For convenience of computation, the final installation angle of 3° is selected.

4. Performance Estimation

4.1. Lift Estimation

The formulas for calculating lift and drag are as follows:

$$L = 0.5\rho V^2 S C_L \tag{23}$$

$$D = 0.5\rho V^2 S C_D \tag{24}$$

By using the high-lift airfoil MH115, the desired lift coefficient is 0.7564. At a speed of 7.5 m/s, the lift force L is 78.4 N, which satisfies the design requirement of an 8 kg takeoff weight. The drag coefficient is 0.0483075, resulting in a drag force D of 5 N. The power required for level flight is P = 37.55 W. If the flight speed is increased to V = 8 m/s to achieve a lift force of 8 kg, the required lift coefficient is $C_L = 0.6647$, and the drag coefficient is C_D = 0.044584. The power required for level flight is P = 42 W.

For propeller engines, it is evident that increasing the lift coefficient is advantageous for increasing the takeoff weight [42]. Although it may not be in the region of the maximum lift-to-drag ratio, increasing the lift coefficient can reduce the power requirement compared to increasing the flight speed. Based on this principle, theoretical power requirements can be designed and optimized.

Based on the estimation, the relationship between the lift coefficient and drag coefficient for the main wing is presented in Table 7.

Table 7. Relationship between wing lift coefficient and drag coefficient.

Speed	Lift Coefficient	Drag Coefficient	Drag	Power
7.5	0.7563502	0.0483045	5.00704	37.5528
7.6	0.7365772	0.0474322	5.048604	38.36939
7.7	0.7175696	0.0466155	5.093099	39.21686
7.8	0.6992883	0.0458501	5.140434	40.09538
7.9	0.6816968	0.0451322	5.190524	41.00514
8	0.6647609	0.0444584	5.24329	41.94632
8.1	0.6484484	0.0438253	5.298658	42.91913

4.2. Propulsion Power and Climb Requirements

The calculation of aircraft power requirements is a complex process that involves multiple factors and parameters, including the aircraft's design characteristics, flight phases, airspeed, aerodynamic performance, payload, and meteorological conditions. When flying at different speeds, the lift force should be equal to the weight, i.e., L = mg = 78.4. Therefore, the expression for the required lift coefficient is as follows:

$$C_L = \frac{78.4}{0.5\rho V^2 S} \tag{25}$$

The drag coefficient can be expressed as $C_D = C_{D0} + AC_L^2$, and the drag force is given by

$$D = 0.5\rho V^2 S \left[0.0314 + 0.02955 \left(\frac{78.4}{0.5\rho V^2 S} \right) \right] \tag{26}$$

Let us assume the angle of attack is α, and the climb angle is γ. The expression for the required thrust is

$$T = (D + mgsin\gamma)cos\alpha \tag{27}$$

The angle of attack can be obtained based on the required lift coefficient, and there is the following relationship:

$$\alpha = \frac{C_L - C_L^0}{C_L^\alpha} \tag{28}$$

The optimized design theory for the required power can be determined as follows:

$$W_\tau = T \times V \tag{29}$$

Based on the above formulas, we can obtain the power required for level flight at different speeds, as shown in Figure 8.
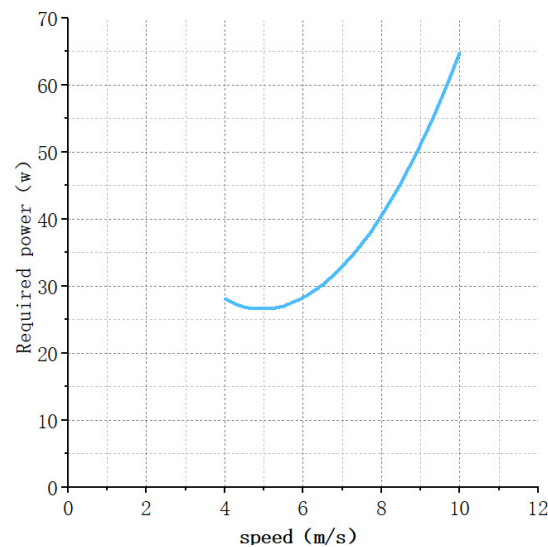

Figure 8. Required power for level flight at different velocities.

From the perspective of power, using a lower speed is more advantageous, as the minimum power required occurs at around 5 m/s. However, at this speed, achieving the required lift (takeoff weight) requires a higher lift coefficient of approximately 1.77. Considering safety factors, the maximum lift coefficient for the airfoil is around 1.6. Hence, the design speed is set at 7.5 m/s, with a power requirement of approximately 36 W for level flight.

4.3. Climb Performance

For different climb rate requirements, the corresponding climb angle can be calculated:

$$sin\gamma = \frac{V_y}{\sqrt{V^2 + V_y^2}} \tag{30}$$

Subsequently, based on the optimized design theory, the required power in the climb phase, denoted as W_τ, can be obtained. Figure 9 represents the power required for climbing corresponding to different climb angles.
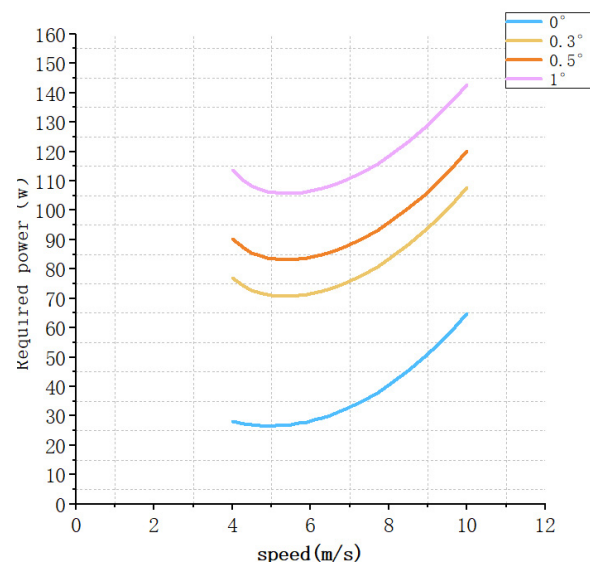
Figure 9. Power required for climbing at different climb angles.

5. Prototype Testing and Flight Testing of the Power System and UAV Platform

Flight testing is essential after the completion of the design optimization of a solar-powered UAV. Flight verification not only validates the correctness of the design theory but also exposes any shortcomings in different aspects of the UAV, enabling improvements and mitigations in future research [43]. In this chapter, based on the detailed design parameters of the UAV presented earlier, a three-dimensional model of the UAV is created using AutoCAD 2021 and Catia V5R21 software. Subsequently, the construction and flight testing of the prototype are conducted, and the results are compared with the design theory.

5.1. Establishment of a Three-Dimensional Digital Model

According to the sketch, a three-dimensional digital prototype is depicted as shown in Figure 10.
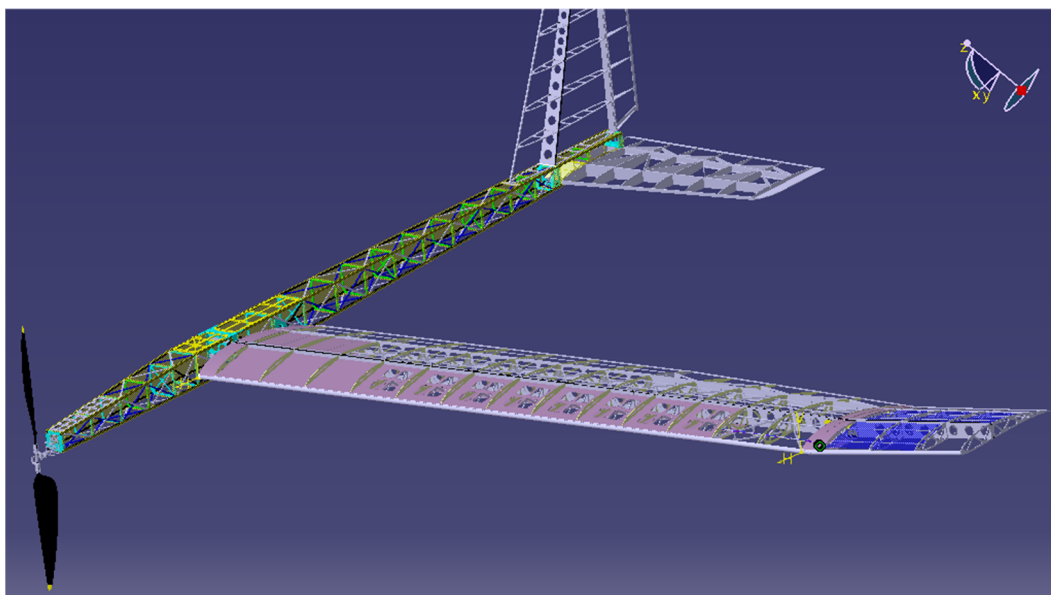

Figure 10. Stereoscopic schematic of the UAV.

5.2. Integrated Design of Solar Panels and Structure

The prototype's wing is primarily composed of wooden materials and carbon fiber composite materials. The main spar utilizes a carbon fiber-wound tube with a diameter of 30 mm and a wall thickness of 0.5 mm. To increase the wing's torsional stiffness, diagonal ribs have been added between the regular ribs and the carbon tube main spar. Adhesive strips are used on the sides of the regular ribs and the upper side of the diagonal ribs for laying the solar panels. Carbon fiber patches are applied to the leading edge, trailing edge, and critical areas, while the bottom skin employs transparent heat-shrink film material. The fuselage is constructed using carbon fiber composite material stringers, laminated frames, and structural side panels, with the stringers oriented in the same direction as the twisting stress in the fuselage, and the overall assembly is bonded. The construction methods for the horizontal and vertical tails are similar to those of the wing and will not be further elaborated.

The solar panels are securely attached to the wing by using double-sided adhesive foam tape at the bottom surface of the panels and attaching them to the wing spars. This serves two purposes: firstly, the foam tape absorbs vibrations during flight and transportation, preventing damage to the solar panels, and secondly, the proximity of the attachment points prevents deformation of the wing during flight, which could potentially cause damage to the solar panels. The solar panels are connected using photovoltaic welding tape, with both the top and bottom surfaces of the panels being welded. Additionally, bypass diodes are welded to each solar panel to prevent any issues with shading or panel failure. Thicker photovoltaic welding tape is used for the wiring connections. Figure 11 illustrates the arrangement of the solar panels on the UAV.
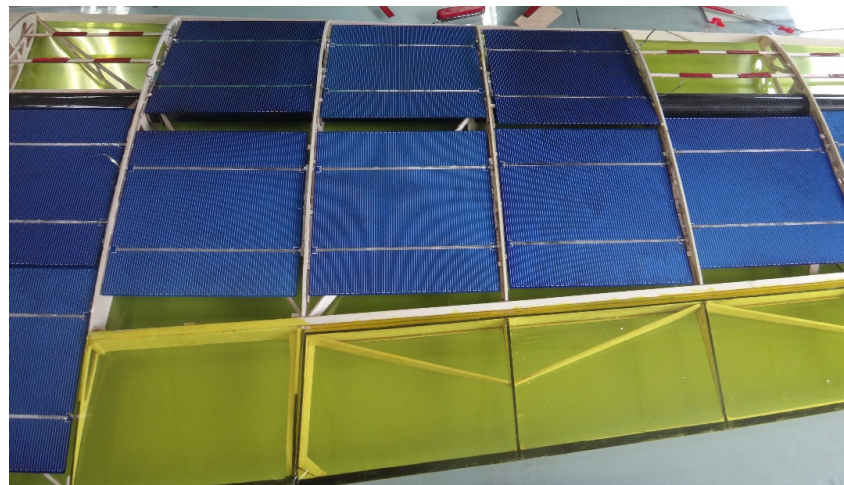

Figure 11. Solar panel installation.

After the completion of the construction of the wooden structure of the aircraft, the upper surface of the wings is covered with high-transmittance, heat-shrinkable, colorless, transparent skin, while the other surfaces are wrapped in yellow transparent heat-shrinkable skin. This approach strengthens the structural integrity of the UAV and helps reduce surface friction drag. Furthermore, the use of high transmittance, colorless transparent skin ensures that sunlight energy is efficiently transmitted to the surface of the solar panels without significant losses. The control surfaces on each wing are connected using nylon hinges. The autopilot, servos, electronic speed controller, and signal receiver, among other components, are all installed within the aircraft. The autopilot utilized is the CUAV V5+, designed based on the Pixhawk FMUv5 standard. However, during the experimental phase, the entire flight is conducted in manual flight mode, and the autopilot functions as an onboard sensor, allowing for flight log analysis through the QGC ground station. The position for the standby battery of the receiver is adjustable, allowing for appropriate adjustment of the center of gravity position. After the center of gravity is adjusted, the

entire UAV is ready for testing. An electronic scale is used to weigh the aircraft, and the total weight is measured to be 2.95 kg, which meets the design requirements.

After the completion of the entire UAV fabrication, it is divided into four main components: two center wing sections, two outer wing sections, the fuselage, and the horizontal tail. This allows for convenient and efficient transportation of the 5.5 m wingspan UAV. Additionally, if any component is damaged, it can be replaced individually, effectively avoiding the waste of repetitive construction. The assembled UAV is shown in Figure 12.

Figure 12. Overall UAV configuration.

5.3. Ground Testing

The integration of the propeller, torque mechanism, electric motor, electronic speed controller, and gearbox was tested.

We use a photoelectric tachometer to measure the propeller's rotational speed and a vibration sensor to measure the vibrations induced by the propeller at its operational speed. The test results indicate that when the maximum power is 120 w, the propeller's rotational speed is 1200 RPM. The relationship between speed and power aligns with the propeller's design, and the torque transmission mechanism operates steadily and reliably. At the operational speed, the vibration amplitude is less than 20 μm, and the cyclic vibration frequency is low, ensuring the propeller's dynamic balance is reliable.

The wing–body junction is the most vulnerable part of the drone's structure, which may fracture upon impact, the material may incur damage under excessive stress, and design flaws could lead to fatigue or vibration issues. Therefore, a static load test was conducted on the wing–body junction of the drone, where it was subjected to a load of 11.9 kg. While the structure experienced significant deformation, it still had load-bearing capacity, and it can be considered that the structural strength would not lead to an in-flight disintegration of the drone.

5.4. Flight Testing

After the completion of the UAV fabrication, field flight tests were conducted on a day with favorable weather conditions. Based on theoretical requirements and practical considerations, the following flight test missions were established:

- Empty aircraft flight verification: this test aimed to validate the trim, maneuverability, and stability of the UAV.
- Flight verification with payload: this test aimed to verify the climb rate of the UAV under certain payload conditions, comparing it with the theoretical calculations.

The flight test is shown in Figure 13.

Figure 13. Empty aircraft flight verification and 4 kg payload flight verification.

6. Comparison of Validation Flight Results with Theory

6.1. Results of Empty Aircraft Test Flight

The flight test results are as follows:

During the unmanned aerial vehicle's (UAV) airframe verification flight phase, for safety reasons, hand-launch takeoff is employed, followed by completing hovering, climbing, and unpowered gliding maneuvers before a safe landing. The CUAV V5+ is equipped with an inertial measurement unit (IMU). Flight logs downloaded from the QGC ground station reveal that during the UAV's level flight phase, the pitch and roll angles do not exceed 2.5°, and the yaw angle does not exceed 4°, as shown in Figure 14. The maximum cruising speed is 7.4 m/s. These observations indicate that the UAV is appropriately balanced, exhibits stable flight performance, offers moderate maneuverability, demonstrates good climbing capability, and maintains a relatively slow flight speed. The propeller performance is excellent, with low power consumption and ample thrust.
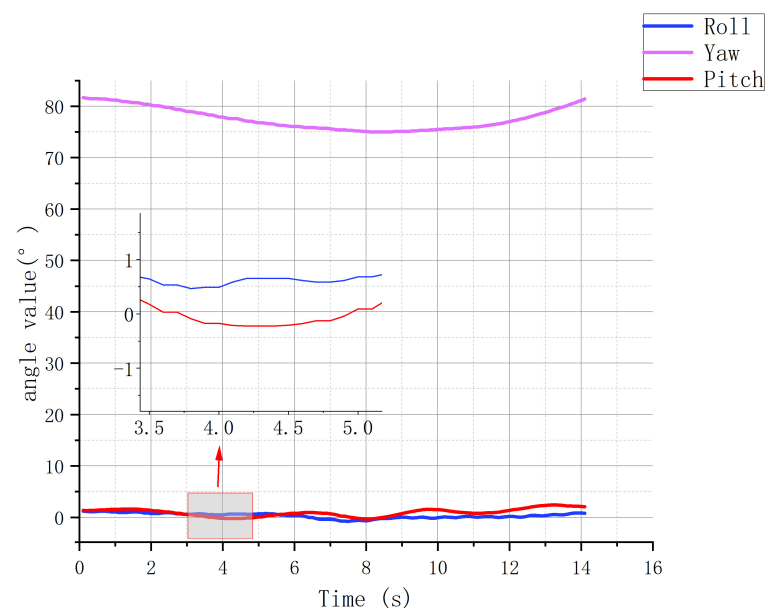

Figure 14. Attitude angle changes during level flight phase.

6.2. Results of Payload Test Flight

Due to inadequate illumination of less than 950 w/m², the flight test for payload validation was conducted with a payload of 4 kg for safety reasons. The test aimed to verify if the energy requirements, as per the design optimization theory, were met. The UAV took off using a runway with a launching cart. After taking off and separating from the cart, the climb rate of the UAV was calculated by estimating the climb height over a certain period of time. This calculation helped determine if the effective power generated by the UAV's propeller met the design requirements. The test results indicated that the UAV, with a payload weight of 4 kg, climbed to an altitude of 100 m in less than 2 min.

To verify the flight results, a comparison is made between the actual flight data and the theoretical calculations for validation. For the loaded flight, with a payload weight of 4 kg and an approximate UAV weight of 3 kg (actual weight of 2.95 kg), the takeoff weight is 7 kg. The climb altitude achieved was 100 m, with a conservative estimate of 2 min for the climb duration.

The actual climb rate can be calculated as follows:

$$V_y = \frac{H}{\Delta t} = 0.83 \text{ m/s} \tag{31}$$

The actual climb rate is determined to be

$$V_x = \sqrt{\frac{2 \times G}{\rho \times S \times C_L}} = 7.7 \text{ m/s} \tag{32}$$

Therefore, the overall speed attained is

$$V = \sqrt{V_x{}^2 + V_y{}^2} = 7.75 \text{ m/s} \tag{33}$$

The climb angle achieved is

$$\theta = \arctan\left(\frac{V_y}{V_x}\right) = 6° \tag{34}$$

The UAV's thrust is

$$T = D + \text{mgsin}(\theta) = 11.38 \text{ N} \tag{35}$$

The actual power generated by the propeller during the flight of the solar-powered UAV is

$$P_{prop} = T \times V = 88.19 \text{ w} \tag{36}$$

According to the optimization design theory, the power required by the propeller, as obtained from the optimization results, is

$$P_{prop-eff} = 100.54 \text{ w} \tag{37}$$

The difference with the actual flight test results is 14.1%. Considering the fact that the sunlight illumination on the day of the test was below the standard condition of 950 w/m², the theoretical calculations should be lower, resulting in a smaller percentage difference. This proves the credibility of the energy calculations in the optimization design scheme; the airframe design matches the power system's output precisely, thereby enhancing the efficiency of the solar-powered drone's power system. This demonstrates the correctness of the design methodology presented in this paper.

7. Conclusions

This paper is based on the independently developed power tracking/power management system. Considering various flight profiles, the required power is selected. The wing area is determined based on the power generation of a single solar panel and wing loading. By comparing energy efficiency and aerodynamic performance, the optimal overall efficiency is the objective for wing geometry optimization. The airfoil design is accomplished using Profili 2.21 software, considering the characteristics of low speed and low thrust-to-weight ratio of solar-powered UAVs while taking into account structural design complexity and trim factors. The body and tail design is performed with the objective of achieving the best aerodynamic performance. Performance estimation and flight testing verification are conducted. The results show that the integrated design method for the body and power system of solar-powered UAVs meets the design characteristics of such aircraft and can precisely match the output power of the solar-powered UAV's power system.

Regarding the integrated design method for the body and power system of solar-powered UAVs, future work can involve further optimization of the wing and body design using CFD methods to ensure the geometry meets various complex airflow conditions. Wind tunnel testing and CFD methods can be used to provide data support and simulation for aerodynamic performance estimation, improving the accuracy and applicability of the theoretical optimization of solar-powered UAV power requirements. In the future, the design of solar-powered UAVs should be approached from a systems optimization perspective, incorporating multiple disciplines such as aerodynamics, structures, controls, and energy. It should consider the development levels achievable in the near, medium, and long term for various subsystem technologies. The next steps in the development of solar-powered UAVs should focus on energy management strategies, comprehensive design techniques for variable layouts, and efficient power systems.

References

1. Noth, A.; Siegwart, R.; Engel, W. Design of Solar Powered Airplanes for Continuous Flight. *Environ. Res.* **2008**, *18*, 21–38. [CrossRef]
2. Jiang, G.; Zhu, M.; Liang, H.; Wu, Z. Reliability Based Multidisciplinary Design Optimization of Solar Powered Aircraft. *J. Nanjing Univ. Aeronaut. Astronaut.* **2012**, *44*, 464–471. [CrossRef]
3. Carmichael, R.; Erickson, L. PAN AIR—A Higher Order Panel Method for Predicting Subsonic or Supersonic Linear Potential Flows about Arbitrary Configurations. In Proceedings of the 14th Fluid and Plasma Dynamics Conference, Palo Alto, CA, USA, 23 June 1981.
4. Panagiotou, P.; Yakinthos, K. Aerodynamic Efficiency and Performance Enhancement of Fixed-Wing UAVs. *Aerosp. Sci. Technol.* **2020**, *99*, 105575. [CrossRef]
5. Sadraey, M.H. *Aircraft Performance: An Engineering Approach*; CRC Press: Boca Raton, FL, USA, 2017; ISBN 978-1-4987-7656-1.
6. Ramanan, G.; Radha Krishnan, P.; Ranjan, H.M. An Aerodynamic Performance Study and Analysis of SD7037 Fixed Wing UAV Airfoil. *Mater. Today Proc.* **2021**, *47*, 2547–2552. [CrossRef]
7. El Adawy, M.; Abdelhalim, E.H.; Mahmoud, M.; Ahmed Abo Zeid, M.; Mohamed, I.H.; Othman, M.M.; ElGamal, G.S.; ElShabasy, Y.H. Design and Fabrication of a Fixed-Wing Unmanned Aerial Vehicle (UAV). *Ain Shams Eng. J.* **2023**, *14*, 102094. [CrossRef]
8. Liem, R.P.; Mader, C.A.; Martins, J.R.R.A. Surrogate Models and Mixtures of Experts in Aerodynamic Performance Prediction for Aircraft Mission Analysis. *Aerosp. Sci. Technol.* **2015**, *43*, 126–151. [CrossRef]
9. Kulfan, B.; Bussoletti, J. "Fundamental" Parametric Geometry Representations for Aircraft Component Shapes. In Proceedings of the 11th AIAA/ISSMO Multidisciplinary Analysis and Optimization Conference; American Institute of Aeronautics and Astronautics, Portsmouth, Virginia, 6 September 2006.
10. Suresh, C.; Ramesh, K.; Paramaguru, V. Aerodynamic Performance Analysis of a Non-Planar C-Wing Using CFD. *Aerosp. Sci. Technol.* **2015**, *40*, 56–61. [CrossRef]
11. Kapsalis, S.; Panagiotou, P.; Yakinthos, K. CFD-Aided Optimization of a Tactical Blended-Wing-Body UAV Platform Using the Taguchi Method. *Aerosp. Sci. Technol.* **2021**, *108*, 106395. [CrossRef]
12. Liu, X.; Zhao, D.; Oo, N.L. Comparison Studies on Aerodynamic Performances of a Rotating Propeller for Small-Size UAVs. *Aerosp. Sci. Technol.* **2023**, *133*, 108148. [CrossRef]
13. Oo, N.L.; Zhao, D.; Sellier, M.; Liu, X. Experimental Investigation on Turbulence Effects on Unsteady Aerodynamics Performances of Two Horizontally Placed Small-Size UAV Rotors. *Aerosp. Sci. Technol.* **2023**, *141*, 108535. [CrossRef]
14. Yang, X.; Ma, D.; Zhang, L.; Yu, Y.; Yao, Y.; Yang, M. High-Fidelity Multi-Level Efficiency Optimization of Propeller for High Altitude Long Endurance UAV. *Aerosp. Sci. Technol.* **2023**, *133*, 108142. [CrossRef]
15. Panagiotou, P.; Kaparos, P.; Yakinthos, K. Winglet Design and Optimization for a MALE UAV Using CFD. *Aerosp. Sci. Technol.* **2014**, *39*, 190–205. [CrossRef]

16. Huang, J. Application and Development Trends of Computational Fluid Dynamics (CFD) Technology and Associated Systems in Aircraft Research and Development. In Proceedings of the 2019 National Conference on Industrial Fluid Mechanics, Taiyun, China, 29–30 June 2019; Fluid Mechanics Professional Committee of the Chinese Society of Mechanics: Beijing, China, 2019; p. 7.

17. He, K.; Mao, Z.; Wang, Q.; Chen, H. Demonstration and validation flight test of scaled aircraft model and its key technologies. *Acta Aerodyn. Sin.* **2017**, *35*, 671–679.

18. Zhang, W.; Guo, Q.; Zhang, Y. Study and Evolvement on Flight Test Technique of Remotely Piloted Subscale Model. *Adv. Aeronaut. Sci. Eng.* **2011**, *2*, 43–47. [CrossRef]

19. Song, L.; Huang, J. The Study of Engine System Selection for Sub-scaled UCAV Flight Test Model. *Aircr. Des.* **2010**, *30*, 38–42. [CrossRef]

20. Sun, M.; Shan, C.; Sun, K.; Jia, Y. Energy Management Strategy for High-Altitude Solar Aircraft Based on Multiple Flight Phases. *Math. Probl. Eng.* **2020**, *2020*, 6655031. [CrossRef]

21. Zhong, W.; Guo, Y.; Zhang, K. Energy strategy on altitude profile for cycle flight of solar powered aircraft. *Acta Aeronaut. Et Astronaut. Sin.* **2020**, *41*, 109–118.

22. Wang, H.; Su, S. An Energy Management Strategy for Long-endurance Solar-powered UAVs. *Technol. Innov. Appl.* **2023**, *13*, 12–16.

23. Slim Abbes, M.; Bouaziz, S.; Chaari, F.; Maatar, M.; Haddar, M. An Acoustic–Structural Interaction Modelling for the Evaluation of a Gearbox-Radiated Noise. *Int. J. Mech. Sci.* **2008**, *50*, 569–577. [CrossRef]

24. Son, O.; Wang, Z.; Gursul, I. Effect of Wing Planform on Plunging Wing Aerodynamics. *J. Fluids Struct.* **2023**, *121*, 103953. [CrossRef]

25. Da Ronch, A.; Ventura, A.; Righi, M.; Franciolini, M.; Berci, M.; Kharlamov, D. Extension of Analytical Indicial Aerodynamics to Generic Trapezoidal Wings in Subsonic Flow. *Chin. J. Aeronaut.* **2018**, *31*, 617–631. [CrossRef]

26. Wu, M.; Shi, Z.; Xiao, T.; Ang, H. Effect of Wingtip Connection on the Energy and Flight Endurance Performance of Solar Aircraft. *Aerosp. Sci. Technol.* **2021**, *108*, 106404. [CrossRef]

27. Gudmundsson, S. Chapter 5—Aircraft Structural Layout. In *General Aviation Aircraft Design*, 2nd ed.; Gudmundsson, S., Ed.; Butterworth-Heinemann: Waltham, MA, USA, 2022; pp. 113–146, ISBN 978-0-12-818465-3.

28. Sandhya, G.; Rishitha, V.S.; Sriram, S.; Sreehari, V. Design and Experimental Structural Analysis of a Solar Powered Aircraft Wing Structure. *IOP Conf. Ser. Mater. Sci. Eng.* **2021**, *1057*, 012027. [CrossRef]

29. Mukhachev, P.; Padalitsa, D.; Ivanov, A. Preliminary Design and Technology Forecast Synthesis for Solar-Powered High Altitude Aircraft. *Proc. Inst. Mech. Eng. Part G J. Aerosp. Eng.* **2022**, *236*, 2225–2234. [CrossRef]

30. Li, S.; Zhou, W.; Luo, J.; Xie, F. An Optimization Method of Overall Design in Small Long-endurance Solar Powered UAV. *J. Air Force Eng. Univ. Nat. Sci. Ed.* **2018**, *19*, 1–8.

31. Wu, M.; Shi, Z.; Ang, H.; Xiao, T. Theoretical Study on Energy Performance of a Stratospheric Solar Aircraft with Optimum Λ-Shaped Rotatable Wing. *Aerosp. Sci. Technol.* **2020**, *98*, 105670. [CrossRef]

32. Ren, Z.; Wang, Z.; Zhang, G. Research on Zero-Lift Drag Estimation Method at Lower Reynolds Numbers. *Aeronaut. Comput. Tech.* **2011**, *41*, 29–31+36.

33. Zhao, L.; Tao, J.; Sun, H.; Sun, Q. Dynamic Modelling of Parafoil System Based on Aerodynamic Coefficients Identification. *Automatika* **2023**, *64*, 291–303. [CrossRef]

34. Xiao, W.; Jin, X.; Wang, Y.; Zhuang, D.; Wang, S. The Effect of Solar-powered Aircraft Wing Airfoil on the Performance of Photovoltaic Modules. *Aircr. Des.* **2022**, *42*, 43–47. [CrossRef]

35. El-Salamony, M.E.; Aziz, M.A. Impact of N-Shaped Wing Morphing on Solar-Powered Aircraft. *Unmanned Syst.* **2021**, *9*, 309–320. [CrossRef]

36. Li, B.; Gao, Y.; Guo, W.; Kang, X.; Meng, H. Design of Lightweight High Aspect Ratio Main Beam for Small Solar-Powered UAV. *J. Nav. Aviat. Univ.* **2017**, *32*, 483–486.

37. Kravchenko, I.F.; Loginov, V.V.; Ukrainets, Y.O.; Hlushchenko, P.A. Aerodynamic Characteristics of a Straight Wing with a Spiroid Wingtip Device. *Trans. Aerosp. Res.* **2021**, *2021*, 46–62. [CrossRef]

38. Que, J.; Wang, W.; Wu, Y. Design of solar-powered aircraft configuration for reducing trim loss. *J. Beijing Univ. Aeronaut. Astronaut.* **2016**, *42*, 1479–1485. [CrossRef]

39. Nicolosi, F.; Della Vecchia, P.; Ciliberti, D. An Investigation on Vertical Tailplane Contribution to Aircraft Sideforce. *Aerosp. Sci. Technol.* **2013**, *28*, 401–416. [CrossRef]

40. Zhang, L.; Ma, D.; Yang, M.; Yao, Y. Overall Design and Sensitivity Analysis of Solar Aircraft Based on Feasible Region Planning Method. *J. Phys. Conf. Ser.* **2022**, *2364*, 012037. [CrossRef]

41. Fioriti, M.; Boggero, L.; Corpino, S.; Prakasha, P.S.; Ciampa, P.D.; Nagel, B. The Effect of Sub-Systems Design Parameters on Preliminary Aircraft Design in a Multidisciplinary Design Environment. *Transp. Res. Procedia* **2018**, *29*, 135–145. [CrossRef]

42. Li, Z.; Zhang, J.; Wu, P. Determination Method for Overall Parameters of Propeller-Based UAV. *Hongdu Sci. Technol.* **2018**, *2*, 24–28.

43. Liu, Z.; Zhang, Y.; Chen, H.; Zhang, Z. Incremental Control System Design and Flight Tests of a Micro-Coaxial Rotor UAV. *Aerosp. Sci. Technol.* **2022**, *131*, 107979. [CrossRef]